Microsecond ramp compression of a metallic liner driven by a 5 MA current on the SPHINX machine using a dynamic load current multiplier pulse shaping

T. d'Almeida, F. Lassalle, A. Morell, J. Grunenwald, F. Zucchini et al.

Additional information on Phys. Plasmas

Microsecond ramp compression of a metallic liner driven by a 5 MA current on the SPHINX machine using a dynamic load current multiplier pulse shaping

T. d'Almeida,[1] F. Lassalle,[1] A. Morell,[1] J. Grunenwald,[1] F. Zucchini,[1] A. Loyen,[1] T. Maysonnave,[2] and A. S. Chuvatin[3]

[1]*CEA, DAM, GRAMAT, F-46500 Gramat, France*
[2]*International Technologies for High Pulsed Power, F-46500 Thégra, France*
[3]*Laboratoire de Physique des Plasmas, Ecole Polytechnique, F-91128 Palaiseau, France*

SPHINX is a 6 MA, 1-μs Linear Transformer Driver (LTD) operated by the CEA Gramat (France) and primarily used for imploding Z-pinch loads for radiation effects studies. Among the options that are currently being evaluated to improve the generator performances are an upgrade to a 20 MA, 1-μs LTD machine and various power amplification schemes, including a compact Dynamic Load Current Multiplier (DLCM). A method for performing magnetic ramp compression experiments, without modifying the generator operation scheme, was developed using the DLCM to shape the initial current pulse in order to obtain the desired load current profile. In this paper, we discuss the overall configuration that was selected for these experiments, including the choice of a coaxial cylindrical geometry for the load and its return current electrode. We present both 3-D Magneto-hydrodynamic and 1D Lagrangian hydrodynamic simulations which helped guide the design of the experimental configuration. Initial results obtained over a set of experiments on an aluminium cylindrical liner, ramp-compressed to a peak pressure of 23 GPa, are presented and analyzed. Details of the electrical and laser Doppler interferometer setups used to monitor and diagnose the ramp compression experiments are provided. In particular, the configuration used to field both homodyne and heterodyne velocimetry diagnostics in the reduced access available within the liner's interior is described. Current profiles measured at various critical locations across the system, particularly the load current, enabled a comprehensive tracking of the current circulation and demonstrate adequate pulse shaping by the DLCM. The liner inner free surface velocity measurements obtained from the heterodyne velocimeter agree with the hydrocode results obtained using the measured load current as the input. An extensive hydrodynamic analysis is carried out to examine information such as pressure and particle velocity history profiles or magnetic diffusion across the liner. The potential of the technique in terms of applications and achievable ramp pressure levels lies in the prospects for improving the DLCM efficiency through the use of a closing switch (currently under development), reducing the load dimensions and optimizing the diagnostics. © *2013 AIP Publishing LLC*. [http://dx.doi.org/10.1063/1.4823720]

I. INTRODUCTION

Producing high energy density states along off-Hugoniot,[1] quasi-isentropic thermodynamic paths in laboratory experiments has been a strong motivation for developing ramp compression techniques for decades. Several different experimental methods were used, ranging from the graded density impactor[2–5] to the high energy explosive techniques.[6,7] Due to the perturbations from shock waves and to the relatively modest pressure levels, the scope of applications of these methods has been somewhat limited.

The relatively recent laser driven isentropic compression techniques[8–11] are among the most promising in terms of both achievable pressure levels and breadth of potential applications. Yet, due to the short pulse durations required to reach high pressure levels, laser-induced ramp waves have shorter rise time and, therefore, sample thicknesses must be limited to typically few tens of microns in order to avoid premature shock formation. Also, difficulties for achieving

uniform laser loading often preclude the use of these techniques for equation of state (EOS) studies.

The development of the High Pulsed Power (HPP) approach has opened new promising avenues for performing Isentropic Compression Experiments (ICE) using intense pulsed magnetic fields. The possibility of high current pulse shaping has significantly lifted previous limitations on sample thickness and geometry.

Over the last decade, numbers of ICE have been conducted, mostly on the Z accelerator at Sandia National Laboratories, on the GEPI generator at the Centre d'Etudes de Gramat-France (now CEA Gramat), and on the compact VELOCE power generator, also operated at Sandia. These experiments have allowed for various material properties studies at pressures up to several hundreds GPa.[12–20] Except for Refs. 19 and 20 which recently reported the ramp compression of a beryllium cylinder, most of these studies were on planar loads. The experiments on the Z accelerator require complex staggered discharge of multiple switches,[21]

guided by extensive Magneto-Hydro-Dynamic (MHD) and Particle in Cell (PIC) simulations,[22] prior to obtaining the desired load current profile.

In this paper, we present a different approach for achieving magnetic ICE on the SPHINX 6MA microsecond Linear Transformer Driver (LTD) and we report the results of an initial set of experiments on a cylindrical aluminum liner. The method requires no change to the generator discharge scheme, and utilizes a very compact pulse-shaping Dynamic Load Current Multiplier (DLCM) inserted in vacuum between the convolute and the ICE load.

Details of the DLCM features are provided in Sec. II. Next, Sec. III discusses both planar and cylindrical ICE load geometries and justifies the choice of the latter for the experiments on SPHINX. Also in Sec. III are shown the results of both 3-D MHD and 1D hydrodynamic simulations accounting for ohmic heating and magnetic diffusion that helped design the cylindrical load. Section IV provides details of the experimental parameters and diagnostics configuration. The main results and analyses are summarized in Sec. V. Section VI gathers the concluding remarks and prospects from this initial work.

II. DYNAMIC LOAD CURRENT MULTIPLIER ON SPHINX

SPHINX[23] is a microsecond LTD generator operated by the CEA Gramat (France) which can deliver a current pulse of 6 MA within 1 μs when fired at a charging voltage of 60 kV. Several options are being evaluated in order to improve the SPHINX performances, including an upgrade to a 20 MA-1μs LTD machine and various power amplification schemes. Within this framework, the DLCM concept proposed by A. Chuvatin[24] is currently being developed. The principle features of the DLCM, described in the schematic Fig. 1(a), are (1) a self-transformer, which serves as a current multiplier whose maximum performance is the doubling of the initial current, (2) a Dynamic Flux Extruder (DFE) with variable impedance, which reduces losses in the stray loop of the transformer and enables current pulse shaping, and (3) a closing switch located upstream of the load which steepens the current rise front. In practice, these functions are fulfilled using the following components: a network of concentric electrodes, a cylindrical wire array, a vacuum convolute with 8 post-holes and a vacuum closing switch.

Figure 1(b) represents the current circulation within this DLCM system. The primary current (purple arrows) injected from the generator through the upper cylindrical co-axial line induces an image current (green arrows). Before switch closure (left part of Fig. 1(b)), the two currents (purple and green arrows) add up and drive the wire array implosion upon a central tube located along its axis, thus, inducing a sharp inductance rise within this region (DFE). This way, the current can be transmitted to the lower inductance load connected to the DLCM exit simply based on inductive division, even without using a closing switch. Therefore, the load current rise front is expected to display an initial slow increase followed by a steeper rise as the current transfer to the load becomes more efficient whilst impedance builds up within
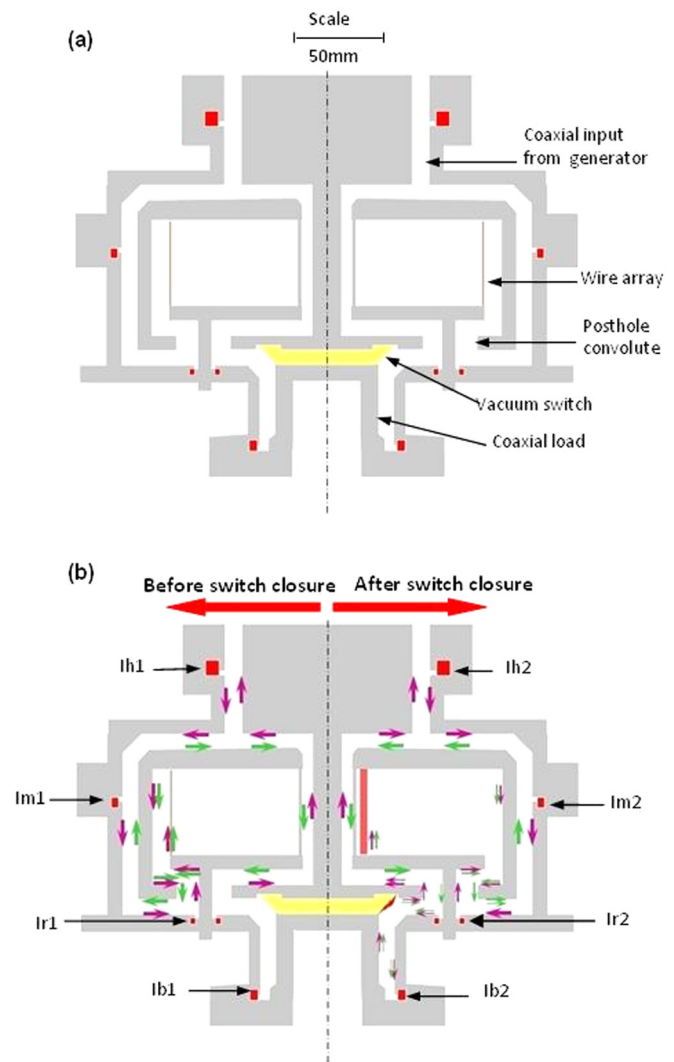

FIG. 1. Conceptual diagram of the DLCM. (a) The upper part represents the cylindrical coaxial line for the current input from the generator. The middle part is made of a network of concentric electrodes and the wire array of the dynamic flux extruder. A switch connected to the posthole convolute separates the DLCM from the coaxial load located in the lower region. (b) The left part of the figure shows the current path before switch closure: primary and image currents (pink and green arrows) add together and drive the wire array implosion, inducing a sharp inductance rise. The right part shows the current path after switch closure, while both current are transferred to the load. Current probes are fielded at various critical locations to ensure current tracking across the system.

the flux extruder. If the DLCM is operated with a switch, the sum current is injected to the load by triggering the switch closure when the desired current level is obtained (right part of Fig. 1(b)). In this case, no current flows through the load until the switch is closed. Upon switch closure, the load current rises sharply within a shorter time and with higher amplitude compared to the initial current delivered by the generator.

In order to monitor the current flow through the system, current probes can be fielded at multiple locations in the higher, medium, and lower parts of the DLCM. In Fig. 1(b), B-dot probes are labeled Ih, Im, and Ib, respectively. Also, Rogowski coils (Ir) can be placed around the post-hole rods in order to monitor the current circulation in this critical region.

Different types of loads can potentially be connected to this DLCM. Among them, wire arrays or gas puff Z pinch loads, for intense X-ray emission, and solids, for magnetic ramp compression experiments, are of particular interest. Both planar and cylindrical ICE load geometries can be studied this way. The motivations for choosing a cylindrical geometry in the work presented in this paper will be discussed in Sec. III.

As a first step and while efforts are underway on the SPHINX machine to optimize a DLCM system equipped with a closing switch[25,26] and operating as described above, the present study was carried out in the microsecond regime, using a cylindrical liner directly connected to the DLCM exit, without closing switch.

III. DESIGN OF THE ICE LOAD

A. Basic considerations for the load design

The time-dependent magnetic pressure exerted upon the ICE load by the local current density is given by

$$P(t) = \frac{B^2(t)}{2\mu_0} = \frac{\mu_0 J^2(t)}{2}, \qquad (1)$$

where $B(t)$ and $J(t)$ are the time-dependent magnetic field and current density at the sample location, respectively; μ_0 is the magnetic permeability of free space.

Magnetic ramp compression experiments are usually carried out on either planar or cylindrical loads; the latter are often referred to as liners. Depending on the load geometry (planar or cylindrical), Eq. (1) expresses the ideal pressure (without losses) as

$$P(t) = \frac{\mu_0}{2} \left(\frac{I(t)}{W} \right)^2. \qquad (2)$$

Here, $I(t)$ is the time-dependent current intensity and W is the width of the planar load; or,

$$P(t) = \frac{\mu_0}{8\pi^2} \left(\frac{I(t)}{R(t)} \right)^2. \qquad (3)$$

Here, $R(t)$ is the time-dependent radius of the cylinder under ramp loading.

Both geometries have advantages and disadvantages for ramp compression experiments. Planar loads allow for higher pressure levels to be reached, as compared to cylindrical loads, for equivalent values of width and initial radius. Also, the planar geometry offers a better access for fielding the diagnostics relevant to dynamic compression experiments, including Doppler interferometers.

On the other hand, the effect of electrodes motion during the ramp compression is likely to affect the loading uniformity and the load current. In the coaxial geometry formed by the cylindrical load and the surrounding return current electrode, unlike in the planar geometry, magnetic field lines tend to close around the liner. Hence, the latter is expected to move perpendicular to its axis during the implosion, which preserves the loading homogeneity. Also, the electrodes

displacement may result in inductance increase and affect the load current intensity and the magnetic pressure. As can be seen in Eq. (3), this drawback is mitigated in a cylindrical geometry through the influence of the term $R^{-2}(t)$ which contributes to pressure enhancement during implosion. The motion of the internal electrode being accentuated towards the end of the ramp, the magnetic field gradient increases, and hence, the required changes to the initial current shape are minimized. Another important requirement for achieving a well characterized ramp loading is to ensure the availability of a sufficiently large one dimensionally loaded area for diagnostics purposes until after peak compression is reached. This area, which must be free of edge wave perturbations, is both current profile and load dimensions dependent. In cylindrical geometry, the only critical dimensional parameter is the length, while the width is equally restricting in planar geometry. The use of a planar load on a long pulsed machine such as SPHINX, with the DLCM operating in the microsecond regime, would entail some practical difficulties. For example, at the start of the ramp loading, edge waves would be launched and would reach the centre of a small planar target before the desired pressure is reached. For an aluminum load, assuming an ambient sound speed of $\sim 6.3 \, \text{km s}^{-1}$, edge waves will have travelled more than 6 mm from each side towards the center at the time of peak current, which imposes a width well above 12 mm to secure a few mm wide undisturbed strip for diagnostics. Such dimensions would significantly lower the achievable peak pressure.

For all the reasons listed above, it appears that the cylindrical geometry befits ramp compression experiments on the SPHINX generator equipped with a DLCM operating in the microsecond regime.

While both geometries are suitable for Isentropic Compression Experiments, they each serve for other specific applications, including magnetically driven flyer plates for shock wave experiments[27–29] (planar geometry), high gain magnetically driven inertial fusion research[30–32] (cylindrical geometry) and instability growth studies in imploding liners.[33–35]

The other important constraints on the design of the ICE load, common to both geometries relate to the mechanisms of shock formation and magnetic field diffusion. Both the current pulse and the load thickness must be tailored to prevent transformation of the stress wave into a shock wave within the sample, while preserving the back surface (opposite to the loading surface) from Joule effect-induced melting over the experimental time scale. The latter condition dictates that the magnetic diffusion depth remains smaller than the sample thickness until all measurements are completed.

Thus, the load thickness results from a compromise between two conflicting requirements: it must be thin enough to avoid shock formation, as compression waves steepen with propagation distance, and thick enough to prevent interaction between reflected waves an magnetic diffusion front, and to preserve the back surface in a solid state, free of magnetic diffusion, until the maximum current is reached and all data are gathered.

To fulfil all these criteria and optimize the experimental configuration, MHD simulations incorporating the physical

properties of the electrodes and all experimental parameters are extremely valuable. These simulations are presented next.

B. Numerical simulations

1. GORGON simulations

MHD simulations were carried out using the numerical 3-D code GORGON[36] in order to simulate the DLCM overall operation and predict the load current profile. An equivalent circuit model was coupled to this code to reproduce the current delivered by the SPHINX generator. The GORGON code which simulates the implosion of the wire array of the DFE is also capable of calculating the spatiotemporal distribution of both electric and magnetic fields across the system. Figure 2 shows a schematic of the electrodes configuration used in these simulations. The cylindrical liner (load) is located directly at the DLCM exit and forms a coaxial line with its return current electrode. No switch is inserted between the DLCM and the load. All of the simulations presented here are for the SPHINX machine fired at a charging voltage of 50 kV, a DFE wire array made of 200 aluminum wires of 12.7 μm diameter and 43 mm height. The current pulse shape obtained in this configuration, which was selected after extensive parametric studies and several test experiments, befits, as it will appear, ramp compression experiments for the desired stress level ($\sim$20 GPa) on an aluminium liner, whose design is described further below.

A set of "numerical" current and voltage probes are simulated at various critical locations across the system; in particular in the current injection gap, in the plane located halfway down the wires of the dynamic flux extruder, in the vacuum convolute region (around the 8 post-hole rods) and within the gap surrounding the liner. As indicated in Fig. 2, a total of 18 current and 14 voltage probes were numerically fielded at multiple locations, using an approach briefly described hereafter.

Numerical current probes are generated by calculating the B field flow $\oint \vec{B}.\vec{dl}$ along a circle centered on the symmetry axis (Oz); the intersection of each circle with the (Ox, Oz) plane is represented by the cross marks in Fig. 2. This magnetic flow equals $\mu_0 I_{wa}$, where the "wrap around" current I_{wa} is the sum of all currents crossing the contour which

serves as a frame for its computation. Numerical voltage probes are obtained by integrating the electric field along the bold black lines represented in Fig. 2, and by azimuthally averaging the resulting value. This method provides direct access to the voltage at both ends of the lines.

The simulated profile of the "wrap around" current (I_4) at the flux extruder position is shown in Fig. 3, along with the actual current carried by the plasma, obtained by subtracting the current I_8 circulating along the on-axis central tube. In these simulations, the wire array implosion is allowed up to the time of plasma impact upon the central tube. The sudden drop in the plasma current intensity is due to the sharp inductance rise resulting from the wire array implosion (the precursor plasma reaches the current probe I8; from that moment on, the signal is not interpretable).

Fig. 4 shows the simulated voltage profiles at different locations within the DLCM. All of these profiles exhibit 2 distinctive parts (leaving aside the decay front). The first part, which lasts up to $\sim$500 ns, corresponds to the ablation phase of the wires forming the DFE where the LdI/dt component of the voltage prevails. It shows a nearly constant plateau, except for the probes located within the injection gap (U1). The voltage amplitude on the plateau increases with distance from the short circuit formed by the wire array (as inductance increases). The maximum voltage is observed around the injection gap, while the minimum occurs at the wire array initial position. The plateau is followed by a rising front corresponding to the plasma implosion phase where the IdL/dt component prevails. This voltage rise gets steeper near the postholes (U4, U7), towards the load.

The simulated profiles of the input current pulse (current delivered by the generator to the DLCM) and the shaped current delivered to the load are presented in Fig. 5. The inflection in the load current occurring at about 600 ns, 2.2 MA, indicates the onset of wire array compression. At this point, the current transfer to the load becomes more efficient as the DFE to load inductance ratio increases sharply. In this experimental configuration, assuming no current loss upstream of the DLCM (within the LTD stages and at the SPHINX main convolute) and across the DLCM, the shaped peak current should be approximately 6.5 MA when the machine is fired at a charging voltage of 50 kV. Parametric simulations show
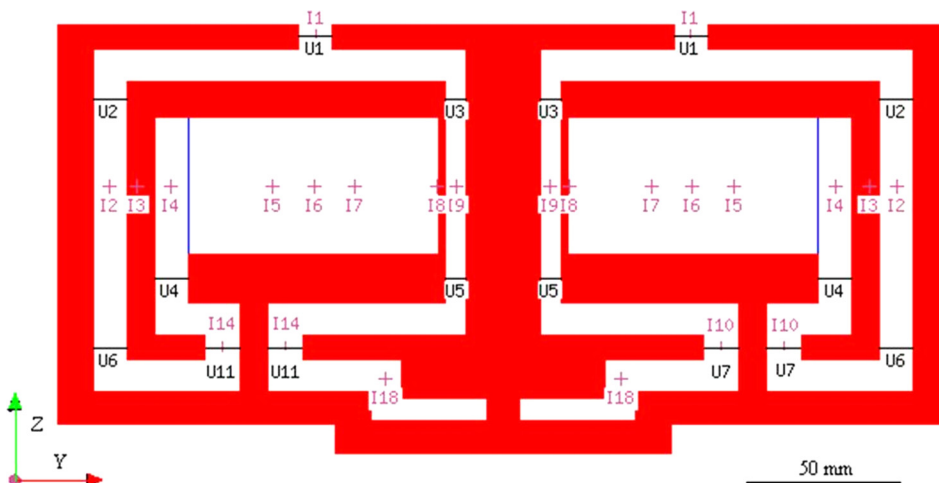

FIG. 2. Sectioned view of the DLCM electrodes configuration used in the 3D MHD GORGON simulations. Numerical voltage (U1 to U14) and current (I1 to I18) probes are fielded at multiple locations across the system.
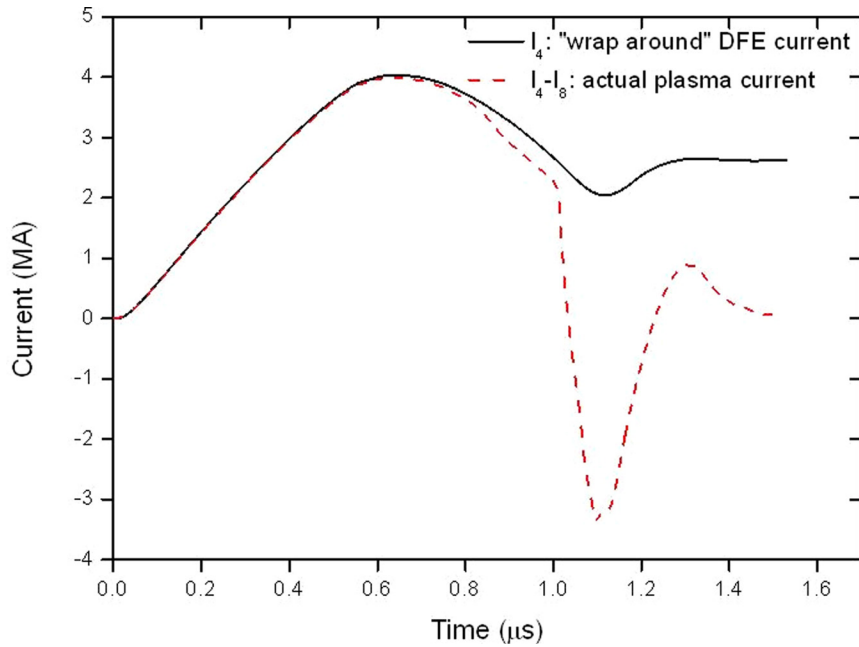
FIG. 3. Simulated profiles of the "wrap around" current (I_4) at the flux extruder and actual current conducted by the plasma ($I_4–I_8$) (GORGON).

that this current profile can be further modified, depending on the desired ramp profile, by adjusting various parameters in the DFE, such as inductance (length of the wires) or mass (number of wires).

As an illustration, Fig. 6 shows the simulated evolution of the load current profile for different lengths of wires, ranging from 30 mm to 70 mm (a length of 43 mm was used in the present study), while the total mass is kept constant by a commensurate reduction of the wire diameter. Such variation of the wire length corresponds to an increase of 0.83 nH in the DFE initial inductance (based on the formula $L = 2 \times l \times \ln(Re/Ri)$, where L is the inductance in nH, l the wire length in cm, and Re and Ri are the outer and inner radii of the coaxial line).

As can be seen in Fig. 6, these simulations suggest that reducing the length of the wire array from 70 mm to 30 mm,

delays the onset of compression (corresponding to the inflection in the load current profile) by ∼120 ns, while reducing the peak current by ∼0.7 MA.

The influence of the DFE mass on the load current profile was also simulated. The results are shown in Fig. 7, for a wire array made of 50 to 300 wires (DFE mass varying from 0.73 mg to 4.41 mg). The simulations suggest that the current rise time, during the wire array compression, may be tuned at some extent, at the expense of a change in peak current. Thus, the DFE mass offers a complementary way of tuning the load current shape.

There is still considerable leeway for improving the DLCM to load current transfer efficiency, as the system is operated here without closing switch. The latter is expected to significantly increase the load peak current, while reducing the foot current down to zero.
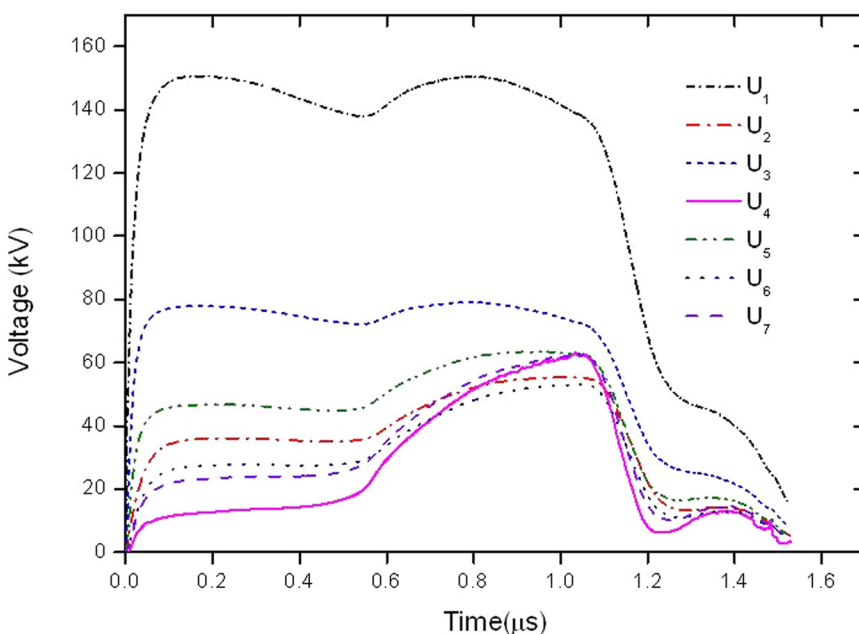

FIG. 4. Simulated voltage profiles at different locations within the DLCM (GORGON).
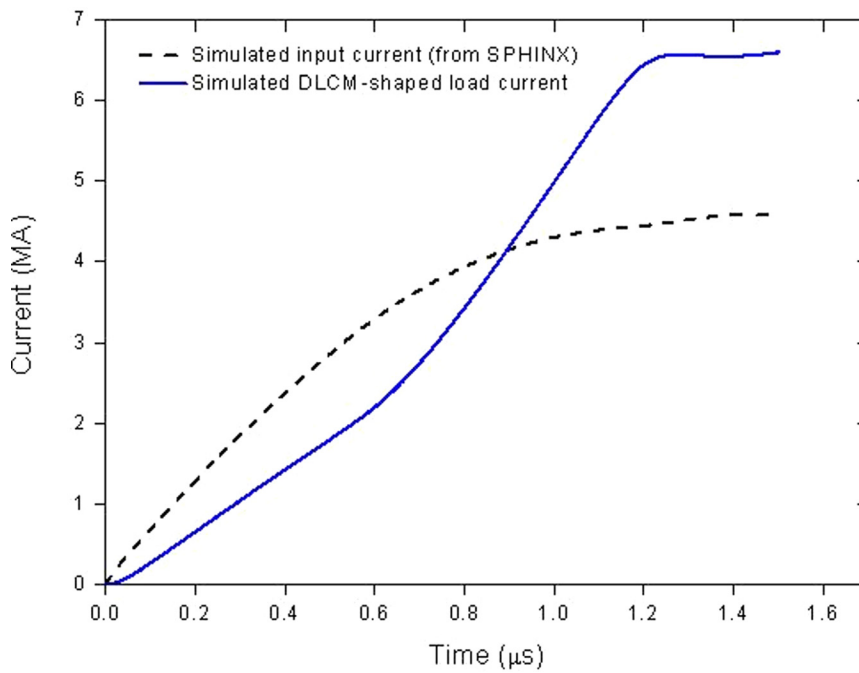
FIG. 5. Simulated DLCM input current pulse and shaped load current (GORGON). The load is a 15 mm tall, 5 mm outer radius, 3 mm inner radius liner. Current losses upstream and within the DLCM are not accounted for.

The above simulations confirm the expected overall features of the DLCM. They provide simulated voltage and current at various critical locations within the system. This information is extremely useful, for example, for locating potential high field regions where extra care in mechanical surface preparation must be taken to prevent unexpected arcing. Gap widening in those regions is not always desirable as it results in inductance increase. Finally, only through MHD simulations can the wire array implosion be analysed and the inductance variation be estimated. So far, this information is not directly amenable to measurements.

2. UNIDIM simulations

Using the load current profile from the GORGON simulations as the input, the magnetic loading of a 5 mm

outer radius, 3 mm inner radius, liner (a detailed load description is provided in Sec. IV) is simulated using the UNIDIM[37] 1D Lagrangian hydrodynamic code developed at the CEA Gramat. This code, based on a finite-difference method and initially inspired from the WONDY V[38] code developed at Sandia National Laboratories, is capable of modelling planar, cylindrical, and spherical load geometries. Although it was initially designed to simulate plate impacts,[39] it has since been upgraded to handle explosive and electromagnetic loadings. The code solves Maxwell equations and simulates both the magnetic diffusion and stress wave propagation. Electromagnetic effects are simulated by introducing Laplace forces and Joule effect in the momentum and energy conservation, respectively.
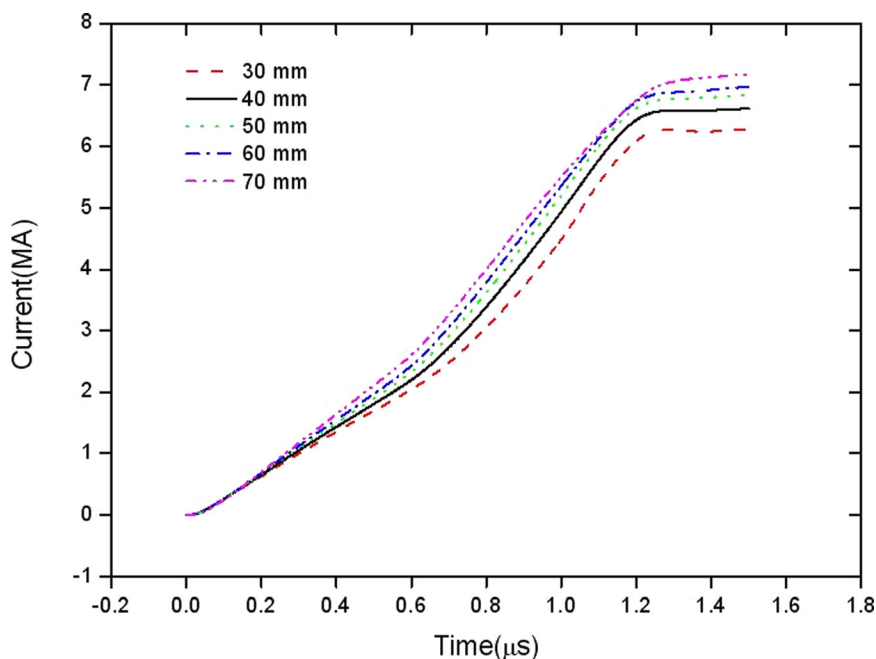

FIG. 6. Simulated load current profiles for different lengths of wires. Increasing the DFE wires length from 30 to 70 mm (at constant mass) increases the DFE initial inductance by 0.83 nH.
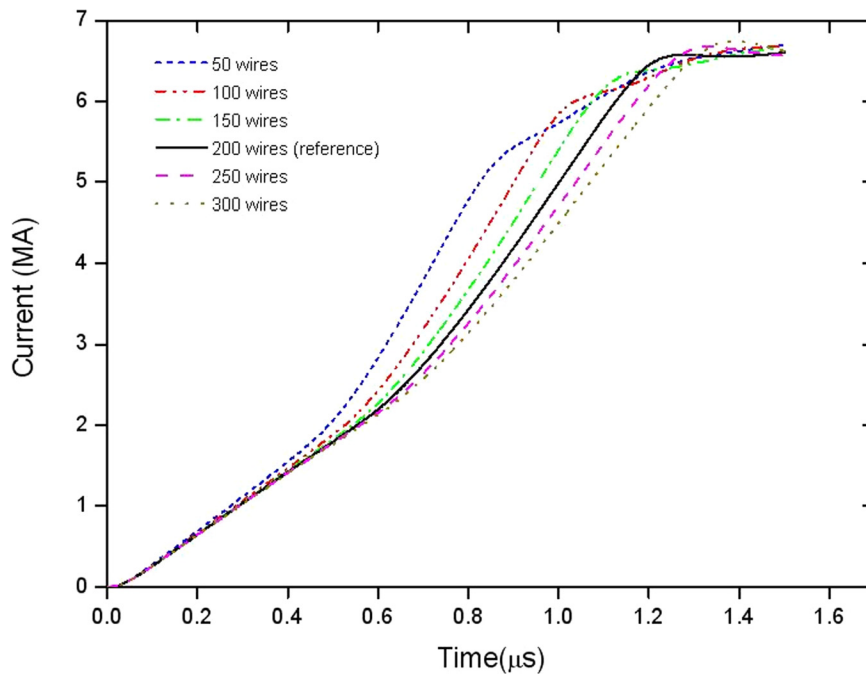
FIG. 7. Simulated load current profiles for wire arrays made of 50 to 300 aluminum wires of 12.7 μm diameter; the corresponding mass variation is 3.68 mg.

UNIDIM is equipped with an extensive EOS library combined with either analytic or tabulated electric and thermal conductivity models for all 3 phases (solid, liquid, and gaseous) enabling the modelling of a large body of hydrodynamic problems. The code is continuously upgraded with new functionalities. The simulations presented here used the Lee-More-Desjarlais conductivity model[40] and the EOS developed by Kerley[41] for pure aluminium and referred to as the SESAME 3700 table.

The output of the UNIDIM hydrodynamic code is valuable for designing, optimizing, and setting up the load experimental configuration. As an illustration, the displacement of the inner free surface is represented in Fig. 8, along with the simulated current at the DLCM exit, which was used as the input. It appears that the inner free surface displacement at peak current is well below 300 μm. Such information is

particularly useful for designing and setting up the velocimetry diagnostics components (described in Sec. IV).

The UNIDIM code also serves for a detailed quantitative hydrodynamic analysis of the experimental data (presented in Sec. V). Using the measured load current as the input, the inner free surface velocity profile can be calculated and compared to the experimental velocity profile.

IV. EXPERIMENTAL CONFIGURATION AND FIELDED DIAGNOSTICS

The overall experimental configuration is shown in Fig. 9. The upper part is made of the DLCM electrodes and the wire array of the DFE whose features were described earlier. The lower part, from the post-hole disc onwards, is comprised of the ICE load unit, the return current electrodes and
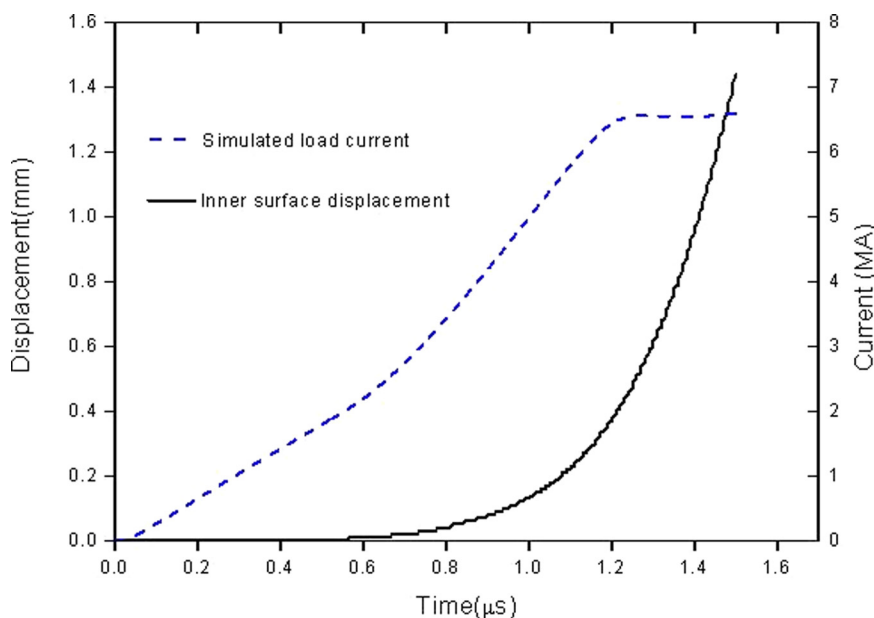

FIG. 8. Simulated shaped load current (GORGON) and liner inner surface velocity (UNIDIM).
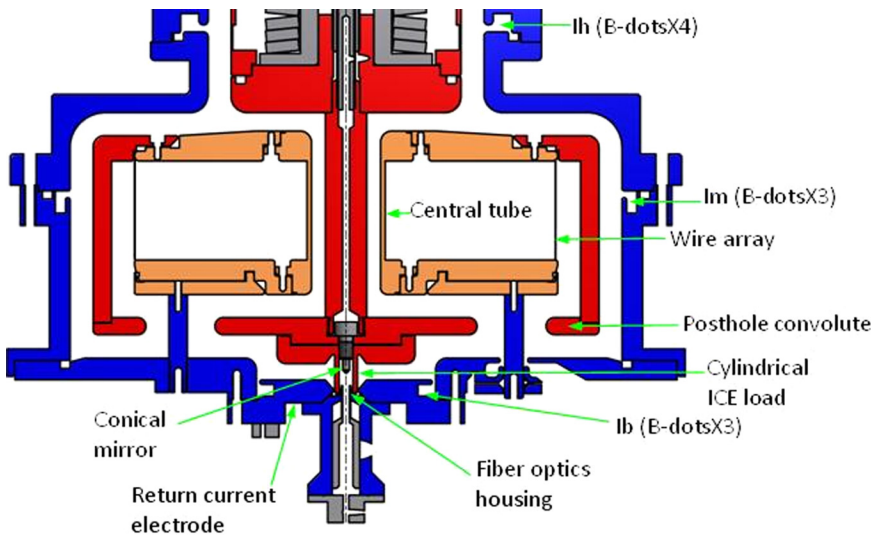
FIG. 9. Sectioned view of the configuration used for the 1 μs ramp compression experiments on the SPHINX machine. The cylindrical ICE load unit is connected directly to the DLCM post-hole disc. B-dot current probes are fielded at multiple locations across the DLCM and within the load return current electrodes. A conical mirror is used (for shots Nos. 811 and 812) to convey a 1550 nm laser beam onto the liner inner surface, and to reflect the returned light to the detectors via a send-and-receive fiber optics.

the housing for the fiber optics head. The load unit, which is bolted to the posthole disc, was machined in one monolithic piece of 6061 aluminum nominally in the T6 treatment conditions. Both outer and inner surfaces were polished down to an arithmetical mean roughness (Ra) of 0.2 μm. The dimensions of this liner load and the gaps downstream of the postholes result from tradeoffs aimed at obtaining a relatively low inductance in the load region and reaching pressure levels of about 20 GPa for these initial ramp compression experiments, while reducing losses (vacuum magnetic insulation) and allowing sufficient space within the liner interior for the diagnostics components. In future experiments, these tradeoffs will be refined further and the detrimental effect of inductance increase on the load current resulting from liner radius reduction will be accurately weighed against the pressure enhancement.

In the present study, the load outer and inner radii were 5 mm and 3 mm, respectively and the corresponding 2 mm thickness was constant along a 16 mm length. An estimated 1-D loaded central strip of length 2 mm (at peak current) was allocated to inner surface velocity measurements. The length of this edge wave free central region at load peak current ($\sim$1.1 μs) was estimated based on a $\sim$6.3 mm μs^{-1} sound speed in aluminum. Optimal electric contact between the liner and the return current electrode was obtained using an annular copper seal strained by the steel unit located at the lower end of the liner which also serves as a holder for the fiber optics head.

Current measurements were fielded at multiple critical locations along the current circulation path, using both B-dot and Rogowski current probes as indicated in Fig. 9. Upstream of the SPHINX main convolute, Rogoswki coils are used to measure the current in all 16 LTD branches. A Rogowski coil is also used to measure the current flowing through the inductive foot which mechanically supports the SPHINX convolute. The current delivered by the generator to the DLCM (Ig) is inferred by subtracting the inductive foot current from the total current measured in all 16 LTD branches. Just upstream of the DLCM, four current measurements Ih$_1$ to Ih$_4$ are carried out within the upper primary return current electrode, using B-dot probes. By subtracting this current from Ig, one

determines the current losses at the main convolute. Within the DLCM, three current measurements, noted Im$_1$ to Im$_3$ are carried out half-way down the outer loop of the transformer, using B-dot probes. Also, four Rogowski coils are fielded around one posthole rod out of two.

In order to infer the current flowing through the load, 3 B-dot probes were placed downstream of the liner, within the return current conductor. These measurements are denoted Ib$_1$ to Ib$_3$.

The B-dot measurements in the load region are very critical in this study since hydrodynamic simulations and data analysis depend upon them as an input.

For calibration purpose, the entire return current electrode equipped with the B-dot probes is inserted within a calibration chamber with a central electrode. The latter is connected as an input to a frequency analyzer, while the B-dot to be calibrated is connected to the output port. This way, the frequency response of each B-dot is measured according to their particular location within the DLCM system. Thus, a frequency correction can be applied to each B-dot measurement obtained during the shot.

The use of such current probes in high current density paths requires that appropriate precautions be taken as to their locations in order to prevent perturbations from electric fields and from possible electrons flow in the transmission lines.[42,43] The reliability of these probes has been extensively tested in SPHINX experiments.[44] As can be seen in Figure 9, in the present study, all B-dots, including the ICE load B-dot probes are recessed in small cavities behind the return current electrodes. Moreover, all B-dot cables are carefully shielded within the SPHINX target chamber.

Current probes are fielded at various critical locations within the DLCM in order to monitor the current circulation across the system. Thus, the consistency of the current measurements can be checked by applying Kirchhoff current laws to the various circuit loops within the system.

In order to measure the inner surface velocity over a broad timeline, a dual laser interferometer using both the homodyne (similar to Velocity Interferometer System for Any Reflector, VISAR[45]) and the heterodyne (Photon Doppler Velocimeter, PDV[46]) techniques was fielded based

on the diagram shown in Fig. 10(a). Due to their complementary features, the combined use of these two interferometric techniques can significantly extend the timescale over which the surface velocity is monitored. The heterodyne interferometer offers the advantage of a better signal to noise ratio. Moreover, even in the case of a noisy signal due to a poor light return, velocity can still be extracted using the Short Time Fourier Transform (S TFT) method. On the other hand, the homodyne technique allows for higher velocities to be measured, while the heterodyne velocimeter is limited by the bandwidth of its components (photodiodes and digitizers).

Figure 10(b) shows details of the optical path within the load section. The optical scheme which is used for the inner surface velocity measurements probes the entire circumference of the liner over a height of 300 μm. The collimated laser beam is incident upon the tip of the conical reflector and reflects towards the inner wall perpendicular to the cylinder axis. Hence, the reliability of this optical probe lays on two key factors: (1) the concentricity between the reflector and the liner axis and (2) the surface quality of both the reflector and liner inner wall.

The choice of this "global" probing method rather than a more localized one in this study was motivated by the need for a mean value of the inner surface velocity. In fact, in this specific experimental configuration, a localized probe is more likely to be affected by possible local imperfections (for example, due to non optimal surface quality or loading uniformity).
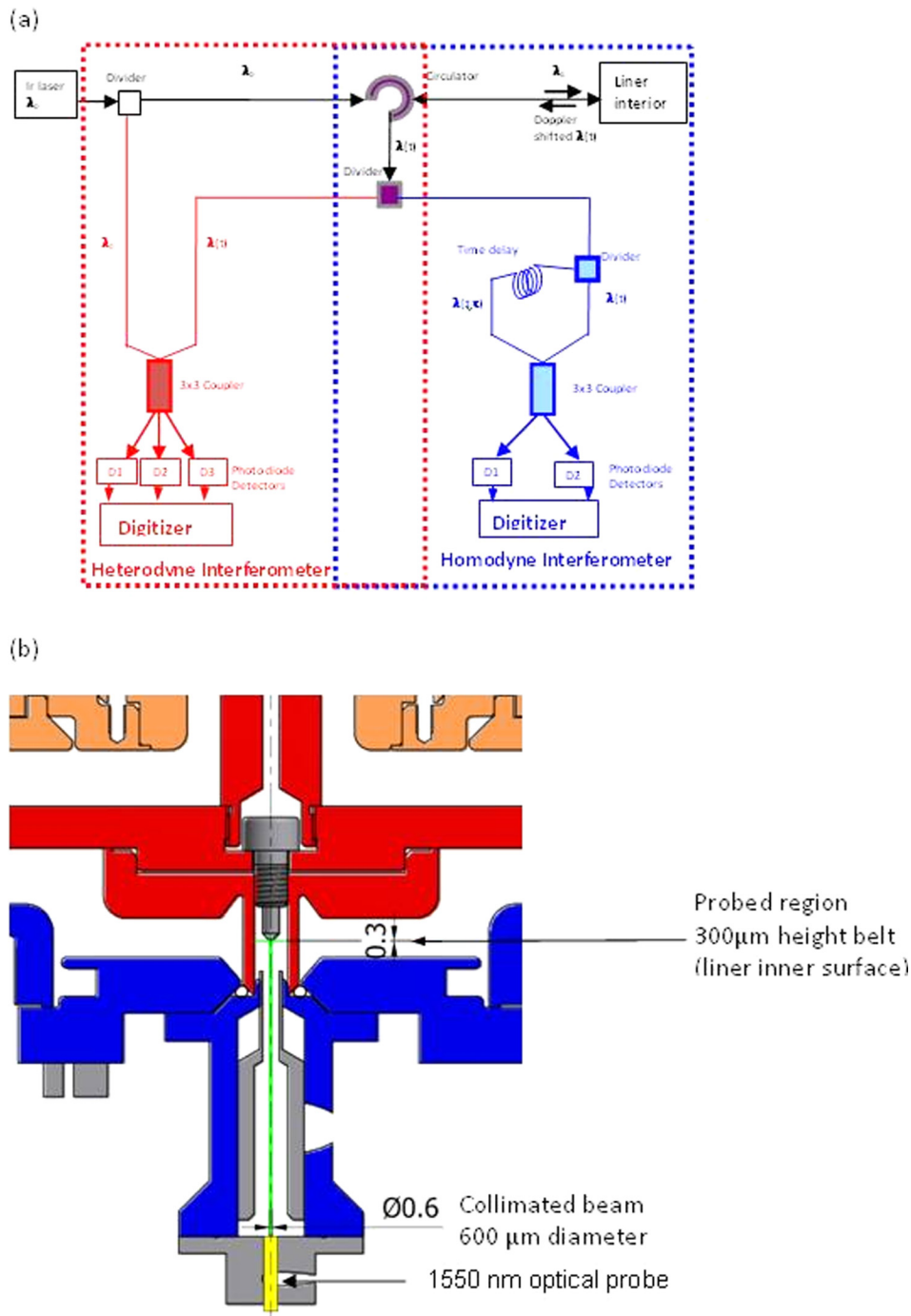

FIG. 10. (a) Schematic of the Doppler interferometry setup used to measure the inner surface velocity of the liner. Both homodyne and heterodyne velocimetry diagnostics were fielded. Due to the low level of the light return, the homodyne signal was not exploitable. (b) Details of the optical path within the load section.

The moving surface is illuminated by the laser beam and reflects a Doppler shifted light. The latter is sent to both interferometers. In the homodyne branch, the returned signal is split into two optical paths, one being delayed. The surface velocity is inferred from the interference of the Doppler shifted lights at times t and t-τ.

In the heterodyne branch, the Doppler-shifted light is recombined to the reference, unshifted beam before detection, thus generating a beat signal which is sent to a digitizer. The displacement and velocity of the moving surface are extracted from the resulting optical phase shift and beat frequency, respectively.

The interferometers use a single continuous wave 1550 nm laser directed via a send-and-receive fiber optics system (OZ-optics, Inc.) onto the inner surface of the liner by a reflector. The latter was machined on the tip of a 3 mm diameter stainless steel rod designed as an extension of the screw which binds the top of the load unit to the DLCM posthole disc. Based on the hydrodynamic simulations presented earlier, this on-axis reflector is expected to remain out of the inner surface trajectory over the signal acquisition timescale.

In the first experiment, the rod tip was flat and cut-oriented at 45° with respect to the cylinder axis. In the following 2 experiments, the rod end was given a conical shape with start and end angles of 44° and 46°, respectively. In both cases, the mirror surface was optically polished in order to optimally reflect the incident and reflected beams. The rod holding screw was sized to position the vertical projection of the mirror surface (1.5 mm height) at the level of the estimated 2 mm high edge waves-free portion of the liner inner surface. In order to minimize possible spurious reflections and to ensure that only the light returned from the liner inner surface is collected, an absorbing black paint was applied to the holding screw and along the steel rod.

An 8 mm diameter focusing optical head with a 50 mm focal length and 0.14 numerical aperture was used in the first experiment. It was later replaced by a collimated fiber of same diameter resulting in a 600 μm diameter illuminated spot on the conical mirror surface. This spot size resulted in a 0.3 mm height probed region at the internal surface of the liner.

Two 400 MHz photodiodes were utilized to detect the back-reflected signal in the homodyne interferometer. These signals were sent to a 2.5 GHz bandwidth TEKTRONIX DP07254 digitizer. The light was split into two legs, one delayed by 12.3 ns with respect to the other, which is suitable for velocity profiles with changes occurring on few hundreds nanosecond timescale.

The heterodyne interferometer system used three detectors in each experiment: three 2 GHz photodiodes were used in the first two shots; two 2 GHz and one 12 GHz photodiodes were used in the last shot. The beat signals from the 2 GHz photodiodes were recorded on a TEKTRONIX DPO7254 digitizer with a bandwidth of 2.5 GHz, and the beat signal from the 12 GHz photodiode was digitized on an 8 GHz bandwidth TEKTRONIX TDS6804B oscilloscope. In principle, these values enable measuring maximum surface velocities of 1550 m s^{-1} and 6200 m s^{-1}, respectively. The total acquisition time was 10 μs.

V. RESULTS AND ANALYSIS

A set of data were obtained over three shots (SPHINX 809, 811, and 812) driven with the generator fired at 50 kV charging voltage. Although the machine is routinely fired at 60 kV on Z-pinch loads, a charging voltage of 50 kV was chosen for the present work in order to reduce the risks of current losses in vacuum due to the higher voltage induced by the equivalent impedance of the DLCM ($Z_{DLCM} > Z_{Zpinch\ load}$). The current reduction resulting from a lower charging voltage was found to be acceptable for these initial experiments. The same DLCM configuration, given in Sec. II, and the same ICE load geometry were used in all three shots.

A. Electrical diagnostics

In the first shot, the electrical diagnostics were all exploitable except for one of the three load current B-dots (Ib). In the second shot, two of the three load current B-dots failed. Nevertheless, the third B-dot probe worked nominally and provided the experimental load current profile. All electrical diagnostics worked properly in the last shot.

Figs. 11(a)–11(c) show the current profiles measured upstream (Ig), and in the upper and middle parts of the DLCM (Ih and Im are obtained by averaging the Ih$_i$ and Im$_i$ values).

The input current from the generator simulated with the equivalent circuit model in the code GORGON is also shown. By and large a reasonable agreement is found between the simulated and measured current upstream of the DLCM, although some discrepancies may be observed in particular in shot No. 811. These discrepancies are most likely due to current losses, not accounted for in the simulation. Further work will be necessary to determine the origin of these losses (main convolute, LTD vacuum lines, LTD stages, etc.).

Simulated and measured load currents in all three shots are shown in Fig. 12. A higher load peak current of 5.45 MA was achieved in the last shot (No. 812). The significantly higher load peak current obtained by simulation (6.56 MA) suggests the existence of current losses within the DLCM, upstream of the ICE load.

B. PDV diagnostic

The homodyne interferometer did not yield any exploitable signal throughout the experiments, while the heterodyne measurements were successful in two shots out of three. This can be explained if one considers the dependency of both signals on the Doppler shifted light intensity. The homodyne signal intensity depends upon the sole returned light intensity, while the heterodyne signal mixes both unshifted and Doppler shifted components. Therefore, the homodyne measurements are more likely to be affected in cases where the light returned from the moving surface is weak.

Thus, the discussion hereafter focuses on the heterodyne PDV results.

In the first shot (No. 809), the light return from the liner inner surface was lost prematurely during the implosion, so
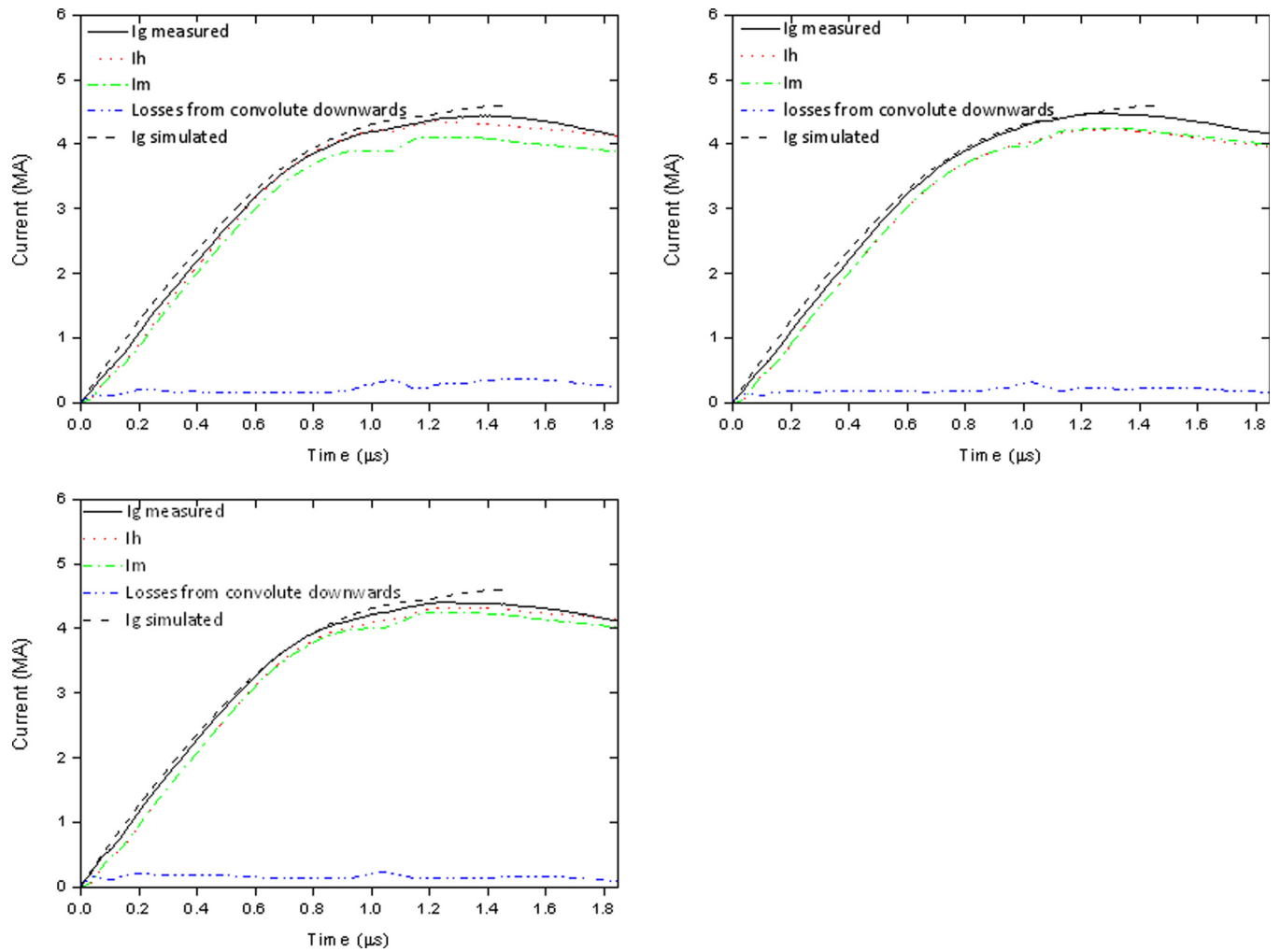
FIG. 11. Current profiles measured upstream (Ig), and in the upper and middle parts of the DLCM (I_h and I_m are obtained by averaging the Ih_i and Im_i values) for (a) shot No.809, (b) shot No. 811, and (c) shot No. 812.

the PDV signal was not exploitable. This measurement was later successful in the following two shots (Nos. 811 and 812): two changes between the first shot and the last two are noteworthy to explain this improvement. First, the mirror geometry was changed from flat to conical as described in Sec. IV. Second, the laser output power was increased to 400 mW only during the shots in experiments Nos. 811 and 812, while all of the pre-shot signals were acquired at 250 mW. In shot No. 809, the laser output power was set to 400 mW throughout the experiment (pre-shot and shot). This extended use of a high power beam may have saturated some optical components during the actual shot. Yet, it is difficult to pinpoint which one of these changes was decisive.

The data were processed using both the STFT technique which separately extracts the velocity from the signal recorded by each individual detector, and the phase unwrapping (PU) technique which yields the surface displacement from the two phase-shifted signals recorded on two individual detectors. However, the latter technique required that the high frequency component be filtered out prior to numerical differentiation in order to extract the velocity. This makes the displacement analysis less convenient.

Experimental surface velocity profiles were extracted from the PDV signals up to $1.13\,\mu s$ and $1.17\,\mu s$ for shots Nos. 811 and 812, respectively.

The PDV measurements are likely to be affected by Gabor uncertainty given the relatively low velocity and short time scales on which changes occur. As an example, for a 50 ns time window at a beat frequency of 2.58 GHz corresponding to a velocity of $2000\,\mathrm{m\,s^{-1}}$, the corresponding 0.7% uncertainty on the inferred velocity is satisfactory. However, there is a need for increasing the overlapping between time windows in the STFT treatment in order to reach a reasonable time uncertainty. Figure 13 shows the velocity profile resulting from the STFT analysis of the PDV measurement for shot 812 using a 50 ns hamming window with 95% overlap. This partly motivates our efforts for improving the homodyne measurements in future work.

Beyond $\sim 1.17\,\mu s$, the PDV signal was significantly deteriorated, most likely because the surface velocity was reaching the limit of the detection system bandwidths. The 12 Ghz detector/8 GHz digitizer channel was meant to offset this failure, but due to its low signal to noise ratio and to the weak light return, this third heterodyne branch did not work.
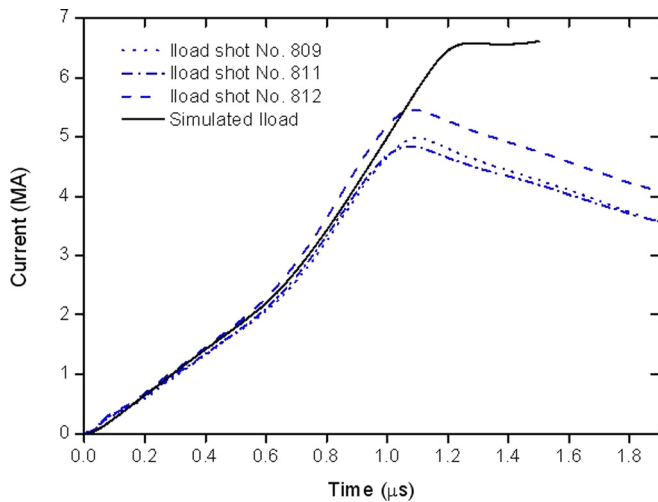
FIG. 12. Measured load current shaped by the DLCM in all three experiments. The simulated load current, also represented, provides an estimate of current losses for each shot.

Further improvements in the surface treatments of the mirror and the liner have since been undertaken to enhance the intensity of the light return in order to achieve simultaneous homodyne interferometric monitoring of the surface velocity in future experiments.

C. Hydrodynamic analysis

Using the experimental load currents as the input, hydrodynamic simulations are carried out using the code UNIDIM. Calculated free surface velocities in UNIDIM are corrected for free surface perturbations.[47]

First, the simulated inner free surface velocities are compared to the measured velocities for each shot. As can be seen in Fig. 14 for shot No. 812, experimental and calculated free surface velocities are in good agreement over the signal acquisition timescale. The inner surface velocity is simulated up to its arrival time on the cylinder axis (1.75 μs for shot No. 812). Due to the deterioration of the light detection from the inner surface, the experimental velocity profile could not be extracted beyond 1.17 μs.

Simulated particle velocity at several Lagrangian coordinates is shown in Fig. 15, along with the inner free surface velocity for shot 812 (the result is qualitatively identical for shot No. 811). The inset represents a zoom that helps distinguishing the time of motion onset for each coordinate. According to these simulations, the inner surface reaches a peak velocity of 14 800 m s^{-1} at the end of implosion 1.75 μs) when its trajectory reaches the cylinder axis.

The release of the stress wave, along the liner outer surface and the melting due to magnetic diffusion, results in a thickness increase and in negative velocity of the outermost coordinate (near the outer surface) beyond $\sim$1.6 μs.

The simulated stress profiles at different Lagrangian coordinates are shown in Fig. 16 for shot No. 812. These profiles nicely illustrate the propagation of release waves, following peak compression, at different depths within the liner.

An attempt is made to try to relate the decay observed in the detected signal from the inner free surface to the propagation of these stress waves. The decay did not occur abruptly at 1.17 μs but actually started from the onset of the inner surface motion. One possible explanation is that the surface reflectivity was altered by ejected matter associated with the arrival of the release wave. However, the simulated innermost stress profile (2 μm from the inner surface) suggests arrival of the release wave at 1.3 μs, that is, 130 ns after a significant decay was already observed in the recorded light return. Therefore, the hypothesis of a surface
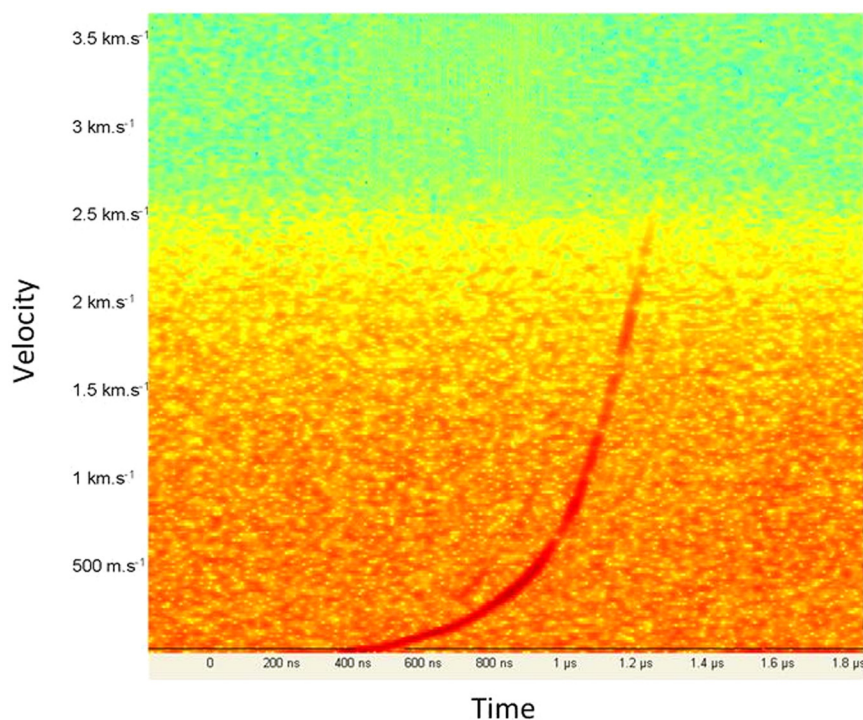

FIG. 13. Surface velocity inferred from the STFT analysis of the PDV measurement for shot 812 using a 50 ns hamming window with 95% overlap.
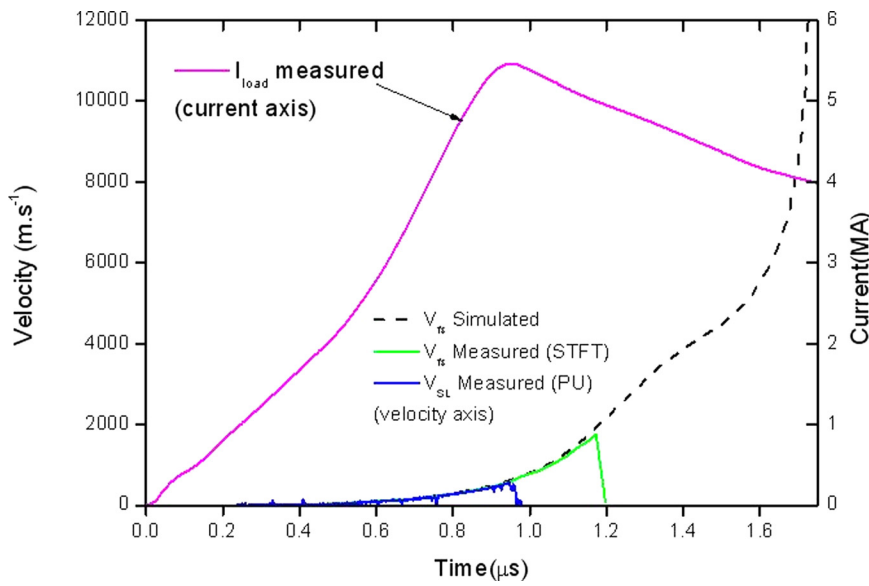
FIG. 14. Surface velocities from PDV measurements (STFT and PU analysis) and from simulation using the measured load current as the input to the hydrocode UNIDIM for shot No. 812, up to 1.17 μs.
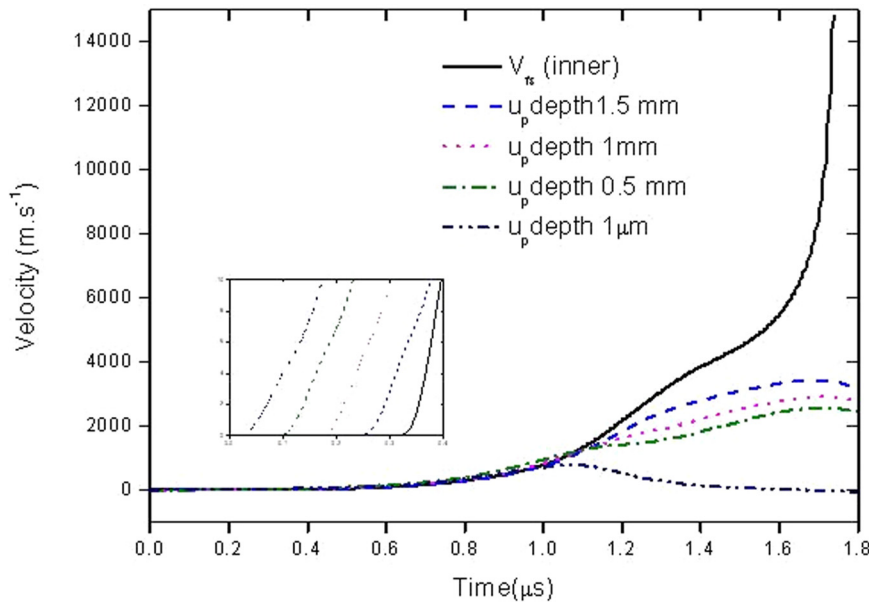

FIG. 15. Simulated inner free surface velocity (V_{fs}) and particle velocities at different Lagrangian positions for shot No. 812. Depths indicate distances from the outer loading surface. The inset helps distinguishing the time of motion onset for each coordinate.
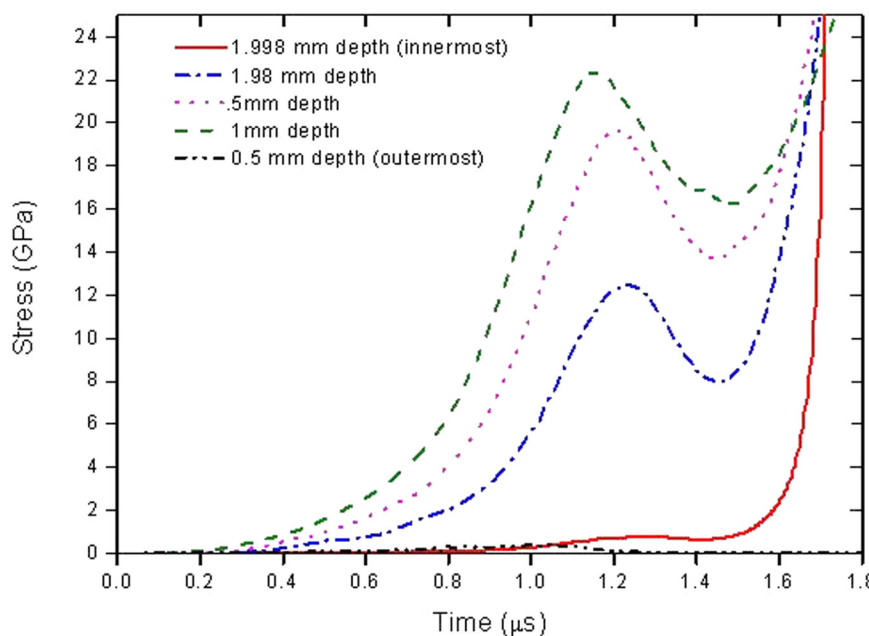

FIG. 16. Simulated stress profiles at different Lagrangian positions. Depths indicate initial distances from the outer loading surface.
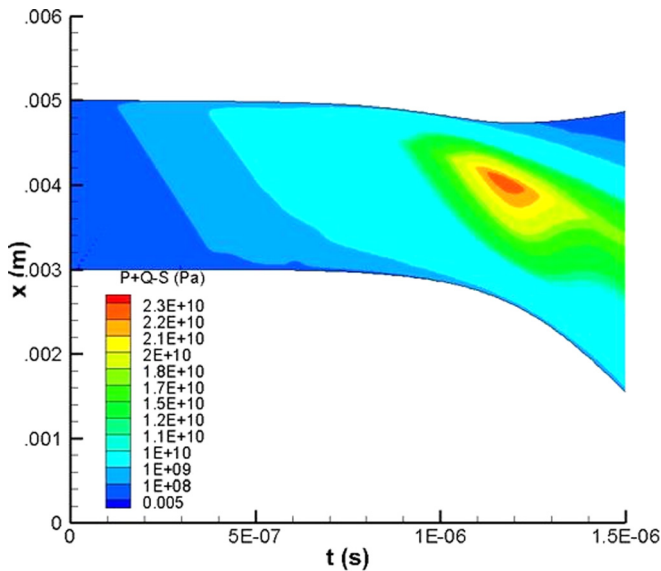
FIG. 17. Simulated stress levels in the liner thickness in X-t diagram for shot No. 812.

FIG. 18. Simulated magnetic diffusion across the liner in X-t diagrams for shot No. 812.

reflectivity drop as a possible origin of the decay in the detected signal is not very likely. Instead, an increase in the surface velocity beyond the system detection limit is more likely. Unfortunately, neither the high bandwidth heterodyne branch nor the homodyne velocimeter which was expected to take over at higher velocities worked. This may be explained by the combination of 2 factors: poor light returned and high surface velocity. This hypothesis will be investigated further in future experiments with an improved surface treatment capable to reflect light at a level suitable for both velocimeters.

Figure 17, which details the results shown in Fig. 16, represents the simulated stress levels within the liner in X-t diagram. A Peak stress of ~23 GPa is obtained toward the middle of the liner thickness for shot 812.

As mentioned earlier, UNIDIM calculates the magnetic diffusion across the liner by coupling Maxwell's equations and Ohm law and by introducing the Lagrangian time derivative of the magnetic field in cylindrical coordinates. The resulting equation is solved considering two boundary conditions: the magnetic field surrounding the liner and the continuity of the electric field inside the liner.[48] The simulated magnetic diffusion is represented in X-t diagrams in Fig. 18 for shot No. 812. Three different regions can be distinguished in the liner, which from the inner surface outward, are (a) a region of virtually null or very weak magnetic field, (b) an intermediate region moderately affected by magnetic diffusion, and (c) a strongly magnetized peripheral region. The simulations show that in the loading conditions of these experiments, the stress wave preceded the magnetic diffusion front in the liner; hence, the material was compressed starting from an initial state not processed by magnetic diffusion. The inner surface remained in a solid state over the experimental timescale.

The simulations indicate that 1.8 mm of the liner thickness (from the inner surface outwards) remains in a solid state up to t = 1.5 μs. The remaining thickness is either liquefied or vaporized. At that specific time, the liner thickness,

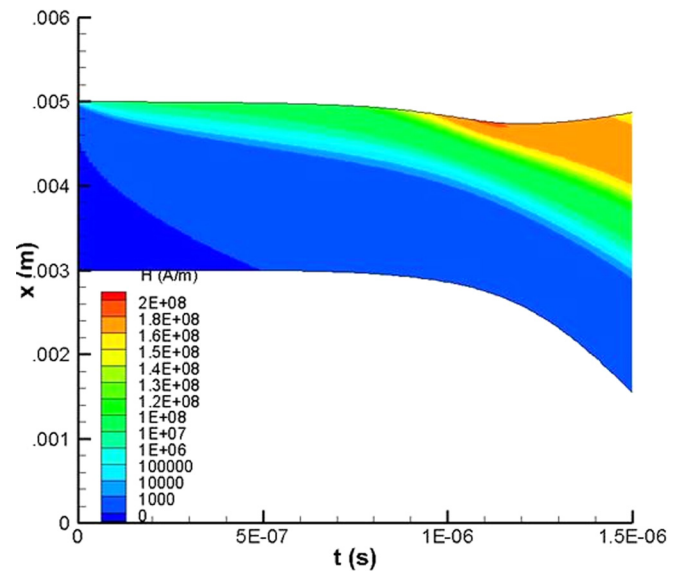all phases considered, is about 2.8 mm. Hence, the proportion of melted thickness is 36% of the total thickness. The velocity of the magnetic front can be estimated to less than 1 mm μs^{-1}, that is, less than 1/6 of the initial sound speed in the aluminium liner.

VI. CONCLUSION

A magnetic loading technique was developed for performing quasi-isentropic compression experiments on the SPHINX microsecond Linear Transformer Driver. This technique is based on current pulse shaping using a compact Dynamic Load Current Multiplier inserted between the SPHINX main convolute and the load and requires no staggering of the generator discharge scheme. In the present work, the DLCM was used in a microsecond regime, with the ICE load directly connected to its exit, without closing switch.

For the first time on this mega-ampere driver, magnetic ramp compression was applied to a cylindrical load whose design was guided by extensive MHD simulations. This co-axial cylindrical geometry befits the SPHINX characteristics and the DLCM configuration developed at the CEA-Gramat.

The fielded electrical diagnostics were valuable for tracking the current circulation across the DLCM unit and accurately measuring the ICE load current. The latter was extremely useful for the post-shot hydrodynamic analysis. An experimental setup which enables direct monitoring of a significant portion of the liner inner surface trajectory through heterodyne PDV interferometry was developed. *In situ* measurements, within the interior of an imploding liner, have been successful only in recent experiments,[49] mainly due to previous difficulties related to reduced access and to various optical alignment issues. The free surface velocity measurements agreed with free surface velocities calculated using the experimental load current as the input to the hydrocode. Further improvements are underway to monitor the

inner surface velocity over a longer timescale using homo-dyne velocimetry.

Although the initial experimental results presented here were obtained at relatively modest peak pressure (~23 GPa), prospects are high for generating Mbar stresses ramp waves on a microsecond driver in the near future, as there is still considerable room for improving the DLCM efficiency through the use of a closing switch and for optimizing the sample dimensions. The present work paves the way for other cylindrical load assemblies on the SPHINX generator. For example, experimental studies of liner instabilities at high strain rates can be foreseen.

Efforts are underway at the CEA Gramat to further develop magnetic loading techniques and related diagnostics capabilities and to extend ramp pressure levels to the multi-megabar regime, in particular in the prospect of a SPHINX upgrade to a 20 MA-1 μs LTD machine,[50] currently under consideration.

Furthermore, coupling the DLCM scheme to various Z-pinch loads will be valuable for improving the performances of the SPHINX X radiation source in the future.

[1]The Hugoniot curve represents the locus of unique end states, each produced by a single, adiabatic and irreversible shock compression, whereas the isentrope is a continuous curve obtained by adiabatic and reversible ramp compression.

[2]L. M. Barker and R. E. Hollenbach, J. Appl. Phys. **41**, 4208 (1970).

[3]W. B. Benedick and J. R. Asay, Bull. Am. Phys. Soc. **21**, 1298 (1976).

[4]L. M. Barker, in *Shock Wave in Condensed Matter-1983*, edited by J. R. Asay, R. A. Graham, and G. K. Straub (Elsevier, New York, 1984), p. 217.

[5]J. H. Nguyen, D. Orlikowski, F. H. Streitz, N. C. Holmes, and J. A. Moriarty, AIP Conf. Proc. **706**, 1225 (2004).

[6]J. F. Barnes, P. J. Blewett, R. G. McQueen, K. A. Meyer, and D. Venable, J. Appl. Phys. **45**, 727 (1974).

[7]J. F. Barnes, D. H. Janney, R. K. London, K. A. Meyer, and D. H. Sharp, J. Appl. Phys. **51**, 4678 (1980).

[8]M. J. Edwards, K. T. Lorenz, B. A. Remington, S. Pollaine, J. Colvin, D. Braun, B. F. Lasinski, D. Reisman, J. M. McNaney, J. A. Greenough, R. Wallace, H. Louis, and D. Kalantar, Phys. Rev. Lett. **92**, 075002 (2004).

[9]K. T. Lorentz, M. J. Edwards, A. F. Jankowski, S. M. Pollaine, R. F. Smith, and B. A. Remington, High Energy Density Phys. **2**, 113 (2006).

[10]D. K. Bradley, J. J. Eggert, R. F. Smith, S. T. Prisbrey, D. G. Hicks, D. G. Braun, J. Biener, A. V. Hamza, R. E. Rudd, and G. W. Collins, Phys. Rev. Lett. **102**, 075503 (2009).

[11]D. C. Swift and R. P. Johnson, Phys. Rev. E **71**, 066401 (2005).

[12]C. Hall, Phys. Plasmas **7**, 2069 (2000).

[13]C. Hall, J. R. Asay, M. D. Knudson, W. A. Stygar, R. B. Spielman, T. D. Pointon, D. B. Reisman, A. Toor, and R. C. Cauble, Rev. Sci. Instrum. **72**, 3587 (2001).

[14]C. Mangeant *et al.*, AIP Conf. Proc. **620**, 1173 (2002).

[15]P. L. Hereil, F. Lassalle, and G. Avrillaud, AIP Conf. Proc. **706**, 1209 (2004).

[16]D. B. Hayes, C. A. Hall, J. R. Asay, and M. D. Knudson, J. Appl. Phys. **96**, 5520 (2004).

[17]JT. Ao, J. R. Asay, S. Chantrenne, M. R. Bare, and C. A. Hall, Rev. Sci. Instrum. **79**, 013903 (2008).

[18]J. R. Asay, T. Ao, T. J. Vogler, J. P. Davis, and G. T. Gray III, J. Appl. Phys. **106**, 073515 (2009).

[19]M. R. Martin, R. W. Lemke, R. D. McBride, J. Davis, and M. D. Knudson, AIP Conf. Proc. **1426**, 357–360 (2011).

[20]M. R. Martin *et al.*, Phys. Plasmas **19**, 056310 (2012).

[21]D. E. Bliss, R. T. Collins, D. G. Dalton, E. J. Dawson, Jr., R. L. Doty, T. L. Downey, H. C. Harjes, E. A. Illescas, M. D. Knudson, B. A. Lewis, J. A. Mills, S. D. Floor, J. W. Podsednik, S. T. Rogowski, M. S. Shams, and K. W. Struve, in *Proceedings of the 14th IEEE Int. Pulsed Power Conference*, edited by M. Giesselmann and A. Neuber (IEEE, Dallas, TX, 2003), p. 179.

[22]T. D. Pointon, H. C. Harjes, M. E. Savage, D. E. Bliss, and R. W. Lemke, *in Proceedings of the 14th IEEE Int. Pulsed Power Conference*, edited by M. Giesselmann and A. Neuber (IEEE, Dallas, TX, 2003), p. 175.

[23]F. Lassalle, A. Loyen, A. Georges, B. Roques, H. Calamy, C. Mangeant, J. F. Cambonie, S. Laspalles, D. Cadars, G. Rodriguez, J. M. Delchié, P. Combes, R. Lample, T. Chanconie, and J. Saves, IEEE Trans. Plasma Sci. **36**, 370 (2008).

[24]A. S. Chuvatin, "Dynamic Current Multiplier," in *14th Symposium on High Current Electronics, Tomsk, Russia* (2006), pp. 232–235.

[25]T. d'Almeida, J. Grunenwald, F. Lassalle, and A. Morell, Technical Report No. DO 173, CEA Gramat, 2012.

[26]T. Maysonnave, F. Bayol, G. Demol, T. d'Almeida, A. Morell, F. Lassalle, J. Grunenwald, A. S. Chuvatin, L. Pecastaing, and A. De Ferron, "Design and testing of a surface switch for the Dynamic Load Current Multiplier on the SPHINX microsecond LTD driver," IEEE Trans. Plasma Sci. (to be published).

[27]R. W. Lemke, M. D. Knudson, C. A. Hall, T. A. Hail, P. M. Desjarlais, J. R. Asay, and T. A. Mehlhorn, Phys. Plasmas **10**, 1092 (2003).

[28]R. W. Lemke, M. D. Knudson, D. E. Bliss, K. Cochrane, J.-P. Davis, A. A. Giunta, H. C. Harjes, and S. A. Slutz, J. Appl. Phys. **98**, 073530 (2005).

[29]R. W. Lemke, M. D. Knudson, and J. P. Davis, Int. J. Impact Eng. **38**, 480 (2011).

[30]V. P. Smirnov, Plasma Phys. Controlled Fusion **33**, 1697 (1991).

[31]S. A. Slutz, M. C. Hermann, R. A. Vesey, A. B. Sefkow, D. B. Sinars, D. C. Rowang, K. J. Peterson, and M. E. Cuneo, Phys. Plasmas **17**, 056303 (2010).

[32]S. A. Slutz and R. A. Vesey, Phys. Rev. Lett. **108**, 025003 (2012).

[33]D. B. Sinars, S. A. Slutz, M. C. Hermann, R. D. McBride, M. E. Cuneo, C. A. Jennings *et al.*, Phys. Plasmas **18**, 056301 (2011).

[34]Peng Zhang, Y. Y. Lau, I. M. Rittersdorf, M. R. Weis, R. M. Gilgenbach, D. Chalenski, and S. A. Slutz, Phys. Plasmas **19**, 022703 (2012).

[35]K. J. Peterson, D. B. Sinars, E. P. Yu, M. C. Hermann, M. E. Cuneo, S. A. Slutz, I. C. Smith, B. W. Atherton, M. D. Knudson, and C. Nakhleh, Phys. Plasmas **19**, 092701 (2012).

[36]J. P. Chittenden, S. V. Lebedev, C. A. Jennings, S. N. Bland, and A. Ciardi, Plasma Phys. Controlled Fusion **46**, B457 (2004).

[37]J. Petit, Technical Report No. CEG T1999-00116/CEG/NC, CEG, 1999.

[38]M. E. Kipp and R. J. Lawrence, Technical Report No. SAND81-0930, Sandia National Laboratories, 1982.

[39]F. Doubax, Ph.D. dissertation, Université Paul Sabatier, 1992.

[40]M. Desjarlais, Contrib. Plasma Phys. **41**, 267 (2001).

[41]G. I. Kerley, Int. J. Impact Eng. **5**, 441 (1987).

[42]T. C. Wagoner, W. A. Stygar, H. C. Ives, T. L. Gilliland, R. B. Spielman, M. E. Johnson, P. G. Reynolds, J. K. Moore, R. L. Mourning, D. L. Fehl, K. E. Androlewicz, J. E. Bailey, R. S. Mroyles, T. A. Dinwoodie, G. L. Donovan, M. E. Dudley, K. D. Hahn, A. A. Kim, J. R. Lee, R. J. Leeper, G. T. Leifeste, J. A. Melville, J. A. Mills, L. P. Mix, W. B. S. Moore, B. P. Peryton, J. L. Porter, G. A. Rochau, G. E. Rochau, M. E. Savage, J. F. Seamen, J. D. Serrano, A. W. Sharpe, R. W. Shoup, J. S. Slopek, C. S. Speas, K. W. Struve, D. M. Van De Valde, and R. M. Woodring, Phys. Rev. ST Accel. Beams **11**, 100401 (2008).

[43]D. V. Rose, D. R. Welch, C. L. Miller, R. E. Clark, E. A. Madrid, C. B. Mostrom, T. C. Wagoner, J. K. Moore, W. A. Stygar, J. E. Bailey, T. J. Nash, G. A. Rochau, and D. B. Sinars, Phys. Rev. ST Accel. Beams **13**, 040401 (2010).

[44]H. Calamy, Technical Report No. T2006-00078/CEG/NC (2006).

[45]L. M. Barker and R. E. Hollenbach, J. Appl. Phys. **43**, 4669 (1972).

[46]O. T. Strand, D. R. Goosman, C. Martinez, and T. L. Whiworth, Rev. Sci. Instrum. **77**, 083108 (2006).

[47]D. B. Hayes and C. A. Hall, AIP Conf. Proc. **620**, 1177 (2002).

[48]J. Petit, Y. A. Alexeev, S. P. Ananiev, and M. N. Kazeev, J. Phys IV France **7**, C3–109 (1997).

[49]D. H. Dolan, R. W. Lemke, R. D. McBride, M. R. Martin, E. Harding, D. G. Dalton, B. E. Blue, and S. S. Walker, Rev. Sci. Instrum. **84**, 055102 (2013).

[50]F. Lassalle, T. Chanconie, B. Roques, and A. Loyen, Technical Report CD No. 3/2012, CEA Gramat, 2012.